

Supplementary Material

H₂-Generation from Alcohols by the MOF-Based Noble Metal-Free Photocatalyst Ni/CdS/TiO₂@MIL-101

Dominic Tilgner,^A Mara Klarner,^A Sebastian Hammon,^B Martin Friedrich,^A Andreas Verch,^{C,D} Niels de Jonge,^{C,E} Stephan Kümmel,^B and Rhett Kempe^{A,F}

^AInorganic Chemistry II, Catalyst Design, University of Bayreuth, Bayreuth 95440, Germany.

^BTheoretical Physics IV, University of Bayreuth, Bayreuth 95440, Germany.

^CINM – Leibniz Institute for New Materials, Saarbrücken 66123, Germany.

^DCarl Zeiss AG, Oberkochen 73447, Germany.

^EDepartment of Physics, Saarland University, Saarbrücken 66123, Germany.

^FCorresponding author. Email: kempe@uni-bayreuth.de

Table of Contents

Experimental Procedures	3
General Methods	3
Material Synthesis	4
General Procedure for Photocatalytic Experiments	6
Material Characterization	8
Photocatalytic Experiments	13
Theoretical Procedures	20
References	24

Experimental Procedures

General Methods

All chemicals and solvents were purchased commercially from chemical suppliers with purity over 95 % and used without further purification. All manipulations including air or moisture sensitive compounds were carried out under dry and oxygen-free argon atmosphere (Schlenk techniques) or in a nitrogen-filled glovebox (mBraun 120) with a high-capacity recirculator (below 0.1 ppm of oxygen and water).

Elemental analysis was performed by standard protocols employing microwave assisted digestion (7 min at 170 °C (80 % power), 7 min at 180 °C (85 % power), and 20 min at 195 °C (90 % power)) in HCl (32 %, 4.5 mL), HNO₃ (65 %, 1.5 mL), and HF (40 %, 1.0 mL). The resulting solution was analysed by inductively coupled plasma optical emission spectrometry (ICP-OES) using a Vista-Pro radial (Varian). Fourier transform infrared (FTIR) spectroscopy measurements were performed with a Cary 630 FTIR spectrometer (Agilent Technologies) over a range from 2000 cm⁻¹ to 550 cm⁻¹. Gas chromatography (GC) analyses were performed using an Agilent Technologies 6850 gas chromatograph equipped with a flame ionization detector (FID) and a MN Optima 17 capillary column (30.0 m x 0.32 mm x 0.25 μm) using n-dodecane or n-decane as internal standard. GC-MS analyses were performed using an Agilent Technologies 6890 gas chromatograph with a MN-MS HP-5 capillary column (30.0 m x 0.32 mm x 0.25 μm) and a coupled mass spectrometer as detector. Gas mixtures were analysed using a 6890N gas chromatograph (Agilent Technologies) equipped with an Agilent special Plot + Molsieve capillary column (30.0 m x 0.32 mm x 0.25 μm). Methane was used as internal standard. Nitrogen physisorption isotherms were determined at -196 °C using a Nova 2000e (Quantachrome) apparatus. Specific surface areas (SSA) were calculated by using p/p₀-values from 0.05-0.25 by the BET model. Specific total pore volumes were measured by DFT calculations (N₂ at -196 °C on silica (cylindr. pore, NLDFT equilibrium model)). Transmission electron microscopy (TEM) measurements were carried out using a LEO 922O microscope (Zeiss, 200 kV). The samples were suspended in chloroform and sonicated for 5 min. 2 μL of the suspension were placed on a CF200-Cu-grid or a LC200-Cu-grid (Electron Microscopy Sciences) and allowed to dry. TEM micrograph Fig. 1 a was recorded with a 12,500x magnification. High-angle annular dark-field scanning transmission electron microscopy (HAADF-STEM) measurements were performed using an ARM200F (JEOL, 200 kV) equipped with a spherical aberration corrector (CEOS) and an energy-dispersed X-ray analysis (EDX) system (JEOL). HAADF-STEM micrographs (Fig. 1 b, c) were recorded with a magnification of 300,000x and 3,000,000x, respectively. The probe size was 7.0 nm and the probe current was 0.08 nA for all samples. Fig. 1 k is a selected region of Fig. 1 c. Diffuse reflectance ultraviolet-visible spectra were measured using a CARY 300 (Agilent Technologies) with an Ulbricht sphere in the range of 450 to 800 nm. X-ray powder diffraction (XRD) analysis was performed using a

XPRT-PRO diffractometer (Panalytical) (CuK α radiation, 1.54178 Å). The reference card numbers for comparison are 00-021-1272 for TiO₂ and 01-080-0019 for CdS. X-ray photoelectron spectroscopy (XPS) measurements were performed using a Specs Phoibos 150 R6 spectrometer equipped with HSA 3500 and MCD-9 detectors, a Specs Focus 500 monochromator, and a XR50M X-ray source (AlK α , 13 kV, 200 W). Time-resolved photoluminescence studies were carried out with a fluorescence lifetime imaging microscope (FLIM) MicroTime200 (Pico Quant). It is equipped with a picosecond diode laser (485 nm) with adjustable output power (set to 0.5 μ W) and a bandpass filter 520/35 nm. The optical core is an inverted microscope IX 73 (Olympus) with a confocal unit and a piezo stage for z stacks. The data were recorded with a water immersion objective (60 \times , NA 1.2.). A single-photon counting APD module (SPAD) is used. Data acquisition is based on time-correlated single photon counting (TCSPC) performed by a TimeHarp 260 Pico board (Pico Quant). Samples are prepared by spin coating thin films of powder material dispersed in a polystyrene (Mw 200k g/mol) matrix on cover slips (18 mm x 18 mm x 200 μ m). 2 mg of the sample are suspended in a polystyrene / toluene solution (300 μ L, 200 mg/mL). Spin coating is performed at 750 rpm for 15 s, 1500 rpm for 30 s, 3000 rpm for 60 s.

Material Synthesis

Synthesis of MIL-101

MIL-101 was synthesized according to our previous work in order to maintain an average crystallite size of 300 nm.^[S1] chromium(III) nitrate nonahydrate (640 mg, 1.60 mmol), terephthalic acid (265 mg, 1.60 mmol), hydrofluoric acid 40 wt.-% (10 μ L, 0.228 mmol), and deionized H₂O (8.00 mL) were sealed in a 23 mL Teflon-lined hydrothermal autoclave. The mixture was heated for 1 h at 80 °C (heating rate: 1.7 °C min⁻¹) and for 7.45 h at 220 °C (4.7 °C min⁻¹). The reaction mixture was cooled down fast to 160 °C and slowly to 30 °C (cooling rate: 5.4 °C h⁻¹). Excessively crystallized H₂BDC was removed by filtration over a pore 3 filter. The product was separated from the reaction solution by centrifugation (2000 rpm, 45 min). The MIL-101 was refluxed in ethanol/water (90/10 vol.-%) for 15 h and centrifuged (1800 rpm, 45 min) to remove the α -CrOOH impurities and to separate the MIL-101 crystals with different size distribution. The green product was dried under vacuum (10⁻⁴ mbar, 85 °C) (BET: 2820 m² g⁻¹).

Synthesis of TiO₂@MIL-101

TiO₂@MIL-101 was synthesized according to our previous work.^[S2] Dry MIL-101 powder (400 mg) was placed in a two-chamber-tube with titanium(IV) isopropoxide (0.64 mL) separated by a glass frit. The gas phase infiltration of the TiO₂ precursor occurred at 32 °C in dynamic vacuum (10⁻⁴ mbar) for 20 h. The resulting bright green powder was processed in hydrolysis by thermal treatment under H₂O

atmosphere at 80 °C. The material was evacuated (10^{-4} mbar) at 85 °C for 20 h, transferred into a 125 mL Teflon-lined hydrothermal autoclave with 50 mL of deionized water, and heated at 150 °C for 10 h (heating rate: 2.0 °C min^{-1}). After cooling down to room temperature, the material was dried under vacuum (10^{-4} mbar, 85 °C). The Ti precursor infiltration, hydrolysis, and hydrothermal treatment described was performed one more time to yield $\text{TiO}_2\text{@MIL-101}$.

Synthesis of $\text{CdS/TiO}_2\text{@MIL-101}$, CdS@MIL-101 , and CdS/TiO_2

200 mg dry $\text{TiO}_2\text{@MIL-101}$, MIL-101, or TiO_2 (anatase, acquired commercial) was suspended in 35 mL of dimethyl sulfoxide in a 125 mL Teflon-lined hydrothermal autoclave. 250 mg cadmium(II) acetate dihydrate were added and the reaction mixture was stirred for 2 h. The mixture was heated at 180 °C for 10 h (heating rate: 2.5 °C min^{-1}). After cooling down to room temperature, the resulting $\text{CdS/TiO}_2\text{@MIL-101}$ was separated by filtration and washed with ethanol. The material was combined with 40 mL of ethanol and heated at 100 °C for 10 h (heating rate: 1.2 °C min^{-1}) in a 125 mL Teflon-lined hydrothermal autoclave. After cooling down, the material was separated by filtration and dried (10^{-4} mbar, 85 °C).

Synthesis of $\text{Ni/CdS/TiO}_2\text{@MIL-101}$, Ni/CdS@MIL-101 , $\text{Ni/TiO}_2\text{@MIL-101}$, Ni/CdS/TiO_2 , Ni/CdS , and Ni/TiO_2

150 mg dry $\text{CdS/TiO}_2\text{@MIL-101}$, CdS@MIL-101 , $\text{TiO}_2\text{@MIL-101}$, CdS/TiO_2 , CdS (cubic, acquired commercial), or TiO_2 (anatase, acquired commercial) was placed in a two-chamber-tube with bis(cyclopentadienyl)nickel(II) (20 mg) separated by a glass frit. The gas phase infiltration of the Ni precursor occurred at room temperature (25 °C) in static vacuum (10^{-4} mbar) for 20 h. The reduction of the Ni precursor was performed under hydrogen atmosphere (10 bar H_2) at 90 °C for 20 h in a Parr Instruments steel autoclave. The resulting $\text{Ni/CdS/TiO}_2\text{@MIL-101}$ was evacuated (10^{-4} mbar, 85 °C) for 20 h in order to remove former metal ligand recess.

Synthesis of $\text{Pd/CdS/TiO}_2\text{@MIL-101}$

The synthesis of $\text{Pd/CdS/TiO}_2\text{@MIL-101}$ was performed as described for $\text{Ni/CdS/TiO}_2\text{@MIL-101}$ using allyl(cyclopentadienyl)palladium(II) (17 mg). The reduction of the Pd precursor was performed at 10 bar H_2 .

Synthesis of $\text{Pt/CdS/TiO}_2\text{@MIL-101}$

The synthesis of $\text{Pt/CdS/TiO}_2\text{@MIL-101}$ was performed as described for $\text{Ni/CdS/TiO}_2\text{@MIL-101}$ using Trimethyl(methylcyclopentadienyl)platinum(IV) (15 mg). The reduction of the Pt precursor was performed at 10 bar H_2 .

Synthesis of $\text{Au/CdS/TiO}_2\text{@MIL-101}$

150 mg dry CdS/TiO₂@MIL-101 powder was placed in a two-chamber-tube with Chlorocarbonylgold(I) (24 mg) separated by a glass installation. The gas-phase infiltration of the Au precursor occurred at 45 °C in static vacuum (10⁻⁴ mbar) for 20 h. The reduction of the Au precursor was performed under hydrogen atmosphere (20 bar H₂) at 90 °C for 20 h in a Parr Instruments steel autoclave. The resulting Au/CdS/TiO₂@MIL-101 was evacuated (10⁻⁴ mbar, 85 °C) for 20 h in order to remove former metal ligand recess.

General Procedure for Photocatalytic Experiments

General procedure for the photocatalytic hydrogen generation by alcohol oxidation

A 10 mL reaction vial was charged with a magnetic stir bar, Ni/CdS/TiO₂@MIL-101 catalyst (0.6 mg), and alcohol (0.1 mmol). The vial was sealed with a rubber septum, evacuated to remove the air atmosphere, and flushed with argon for 2 min. Dry and degassed acetonitrile (0.3 mL) was added and the vial was further purged with argon for 1 min. The vial was illuminated for 24 h by a 50 W blue LED (470 nm, distance 5 cm, ~15000 lx) and cooled by a fan (Figure S9). The reaction temperature was measured to be 27 °C. N-dodecane (10 µL, 44 µmol) was added as internal standard and the catalyst was separated from the reaction solution by centrifugation (9000 rpm, 9 min) before quantitative analysis by GC. The amount of H₂ evolved was determined by injecting 500 µL of methane as internal standard before LED illumination. The gas phase of the reaction was analysed by GC-TDC. Regarding the oxidation of 2-propanol, 7.7 µL (0.1 mmol) of dry and degassed alcohol were added after the evacuation of the vial and dehydrogenated without solvent.

Benzyl alcohol (0.3 mmol, 31.2 µL) and 0.5 mg catalyst were illuminated for 20 h for the comparison of different catalysts (Figure 2a).

Reusability of the Ni/CdS/TiO₂@MIL-101 photocatalyst

A 10 mL reaction vial was charged with a magnetic stir bar, Ni/CdS/TiO₂@MIL-101 catalyst (4 mg), and benzyl alcohol (0.1 mmol). The vial was sealed with a rubber septum, evacuated to remove the air atmosphere, and flushed with argon for 2 min. Dry and degassed acetonitrile (0.5 mL) was added and the vial was further purged with argon for 1 min. The vial was illuminated for 5 h by a 50 W blue LED (470 nm, distance 5 cm, ~15000 lx) and cooled by a fan (Figure S9). N-dodecane (10 µL, 44 µmol) was added as internal standard and the catalyst was separated from the reaction solution by centrifugation (9000 rpm, 9 min) before quantitative analysis by GC. The catalyst was purified with acetonitrile between the runs.

General procedure for the photocatalytic synthesis of imines

A 10 mL reaction vial was charged with a magnetic stir bar, Ni/CdS/TiO₂@MIL-101 catalyst (1.5 mg), amine (0.1 mmol), and alcohol (0.13 mmol). The vial was sealed with a rubber septum, evacuated to remove the air atmosphere, and flushed with argon for 2 min. Dry and degassed acetonitrile (0.15 mL) was added and the vial was further purged with argon for 1 min. The vial was illuminated for 48 h by a 50 W blue LED (470 nm, distance 5 cm, ~15000 lx) and cooled by a fan (Figure S9). The reaction temperature was measured to be 27 °C. N-decane (10 µL, 51 µmol) was added as internal standard and the catalyst was separated from the reaction solution by centrifugation (9000 rpm, 9 min) before quantitative analysis by GC. The amount of H₂ evolved was determined by injecting 500 µL of methane as internal standard before LED illumination. The gas phase of the reaction was analysed by GC-TDC.

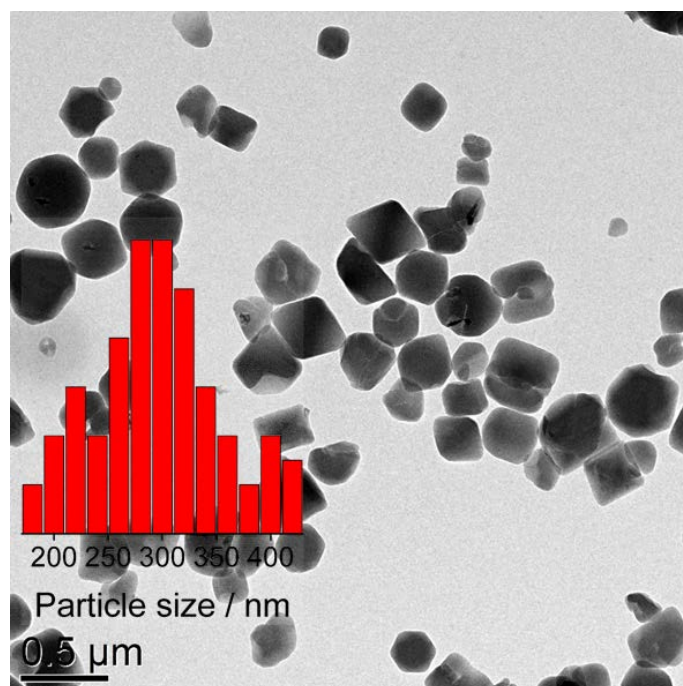


Figure S1. TEM analysis of the as-synthesized MIL-101 crystallites with an average diameter of 300 nm.

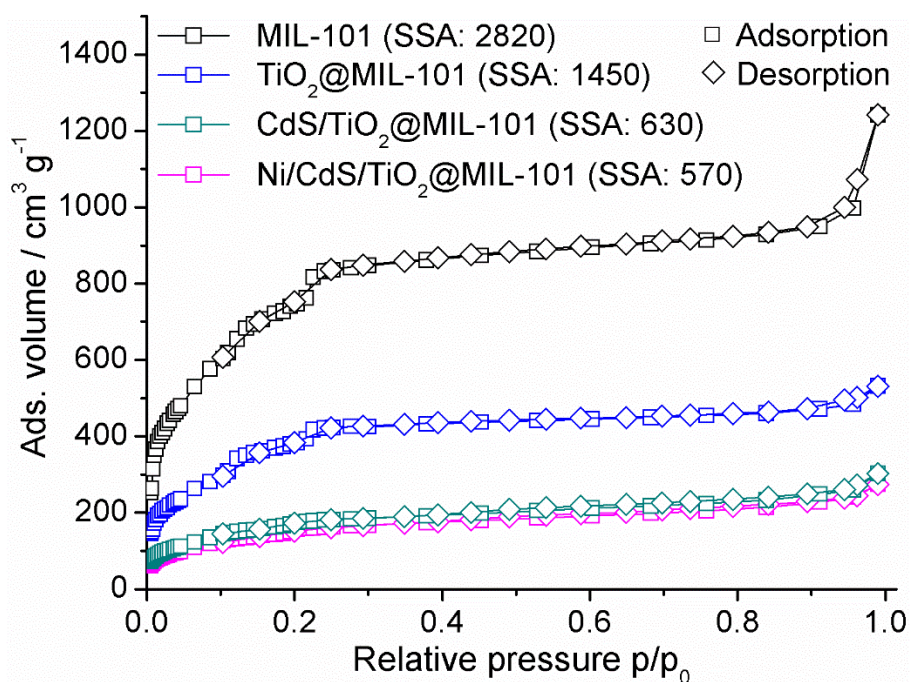


Figure S2. Nitrogen physisorption isotherms of MIL-101, TiO₂@MIL-101, CdS/TiO₂@MIL-101, and Ni/CdS/TiO₂@MIL-101 with the respective specific surface areas (SSA given in m² g⁻¹) determined by the BET model.

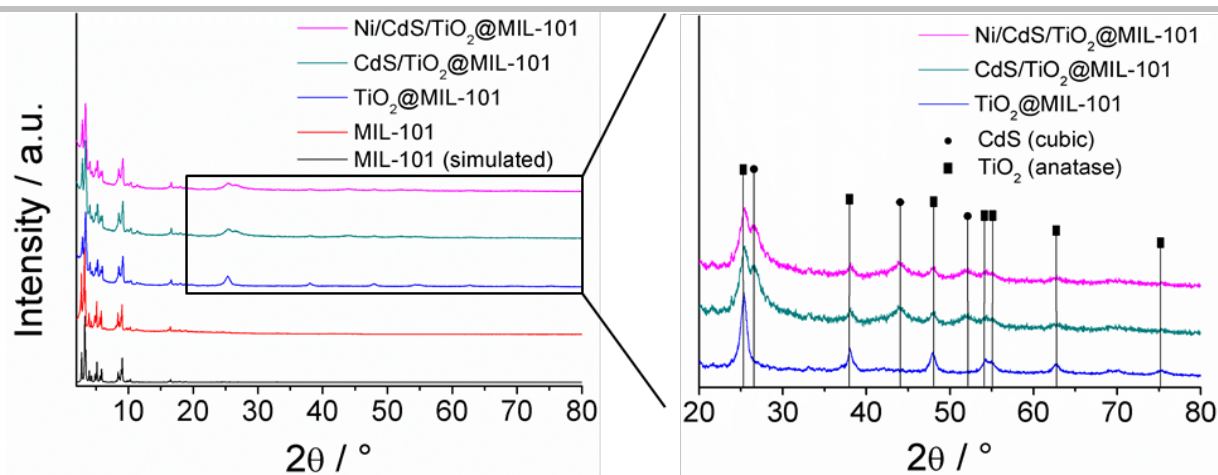


Figure S3. XRD spectra of MIL-101, TiO₂@MIL-101, CdS/TiO₂@MIL-101, and Ni/CdS/TiO₂@MIL-101 with the characteristic reflexes of MIL-101, cubic CdS (Ref. 01-080-0019) and anatase TiO₂ (Ref. 00-021-1272).

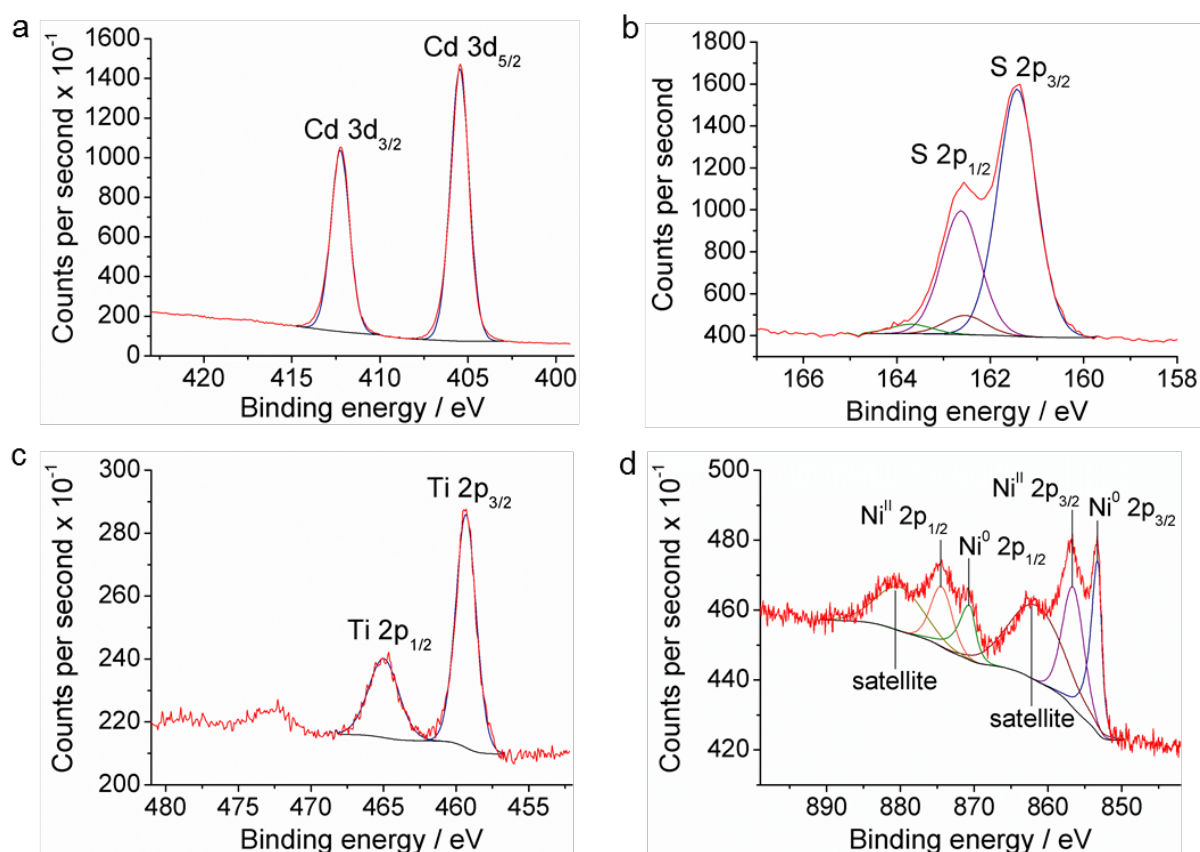


Figure S4. XPS spectra of Ni/CdS/TiO₂@MIL-101 in a) the Cd 3d region, b) the S 2p region, c) the Ti 2p region and, d) the Ni 2p region.

Table S1. ICP-OES analysis of TiO₂@MIL-101, CdS/TiO₂@MIL-101, and M/CdS/TiO₂@MIL-101 (M = Ni, Pd, Pt, Au) with contents given in wt.-%.

Material	Cr	Ti	TiO ₂ ^[a]	Cd	CdS ^[a]	Ni	Pd	Pt	Au
TiO ₂ @MIL-101	11.2	25.0	41.7	-	-	-	-	-	-
CdS/TiO ₂ @MIL-101	7.9	17.8	29.7	16.2	20.8	-	-	-	-
Ni/CdS/TiO ₂ @MIL-101	7.3	15.6	26.0	14.6	18.8	3.6	-	-	-
Pd/CdS/TiO ₂ @MIL-101	6.8	16.4	27.4	15.6	20.0	-	4.3	-	-
Pt/CdS/TiO ₂ @MIL-101	8.2	15.1	25.2	14.3	18.4	-	-	3.1	-
Au/CdS/TiO ₂ @MIL-101	7.1	14.7	24.5	14.8	19.0	-	-	-	5.6

[a] Calculated on the basis of the Ti and Cd content.

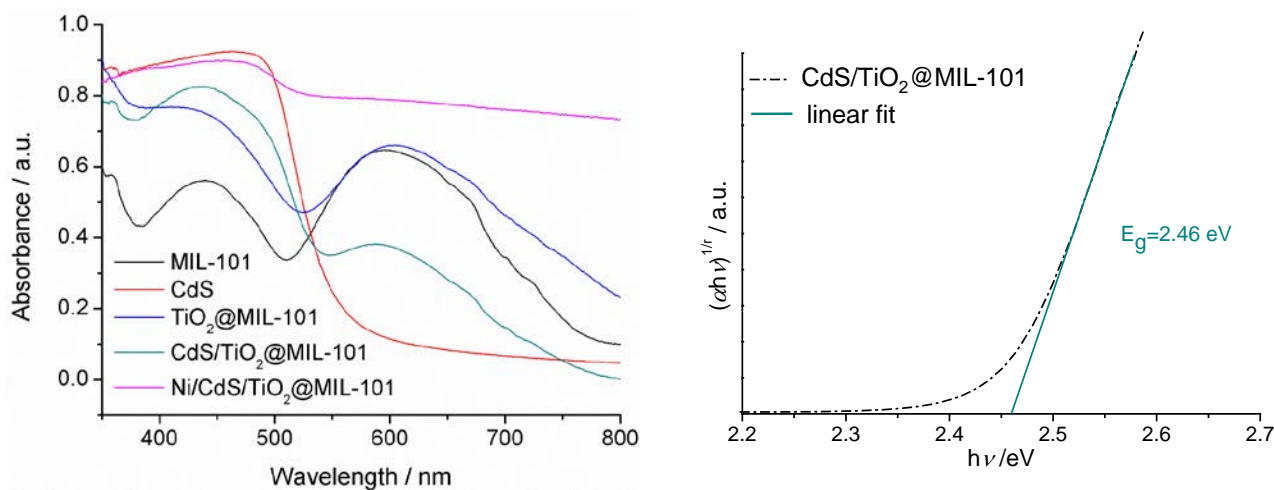


Figure S5. Diffuse reflectance ultraviolet-visible spectra of MIL-101, CdS (cubic), TiO₂@MIL-101, CdS/TiO₂@MIL-101, and Ni/CdS/TiO₂@MIL-101. For CdS/TiO₂@MIL-101, the band gap energy was determined by applying the Munk-Kubelka equation.

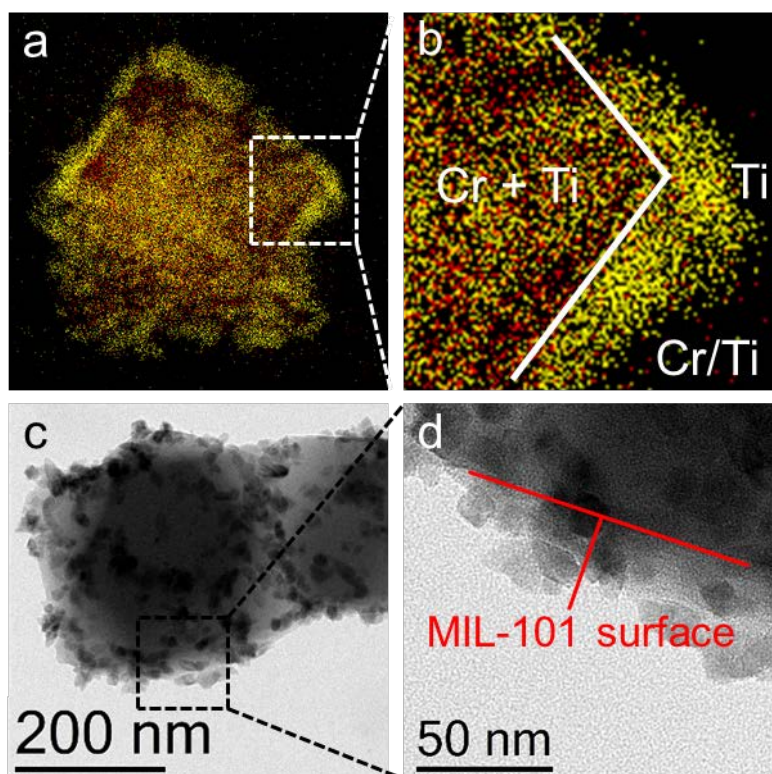


Figure S6. a,b) HAADF-STEM analysis of Ni/CdS/TiO₂@MIL-101 with representative EDX element maps and c,d) TEM analysis of TiO₂@MIL-101 illustrating the core-shell morphology of the materials.

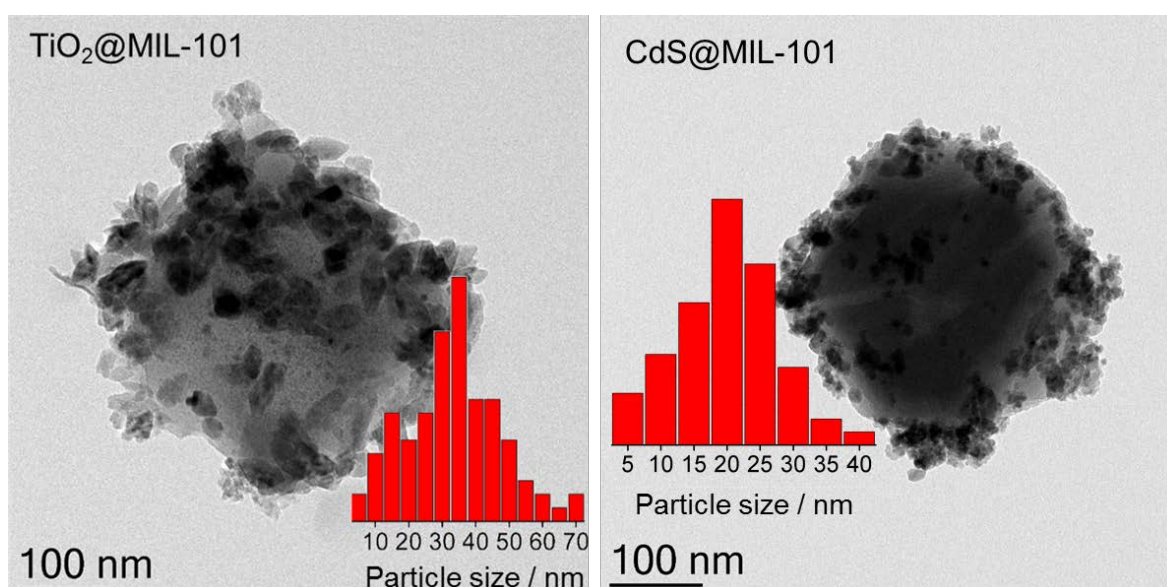


Figure S7. TEM micrographs of TiO₂@MIL-101 and CdS@MIL-101 with the respective particle size distribution.

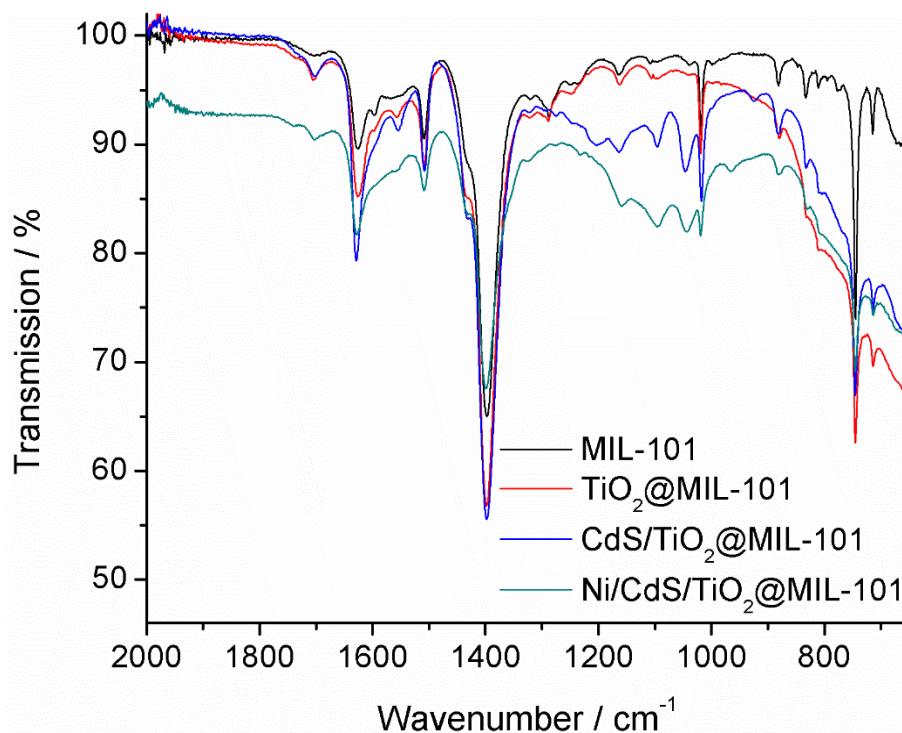


Figure S8. FTIR spectra of MIL-101, TiO₂@MIL-101, CdS/TiO₂@MIL-101, and Ni/CdS/TiO₂@MIL-101.

Table S2. Linear fitting parameters and R²-values (squared correlation coefficient) of the TCSPC traces for the lifetime determination of excited CdS in TRPL studies. The IRF has not been taken into account in the data analysis. Fluorescence lifetimes of CdS catalysts supported on MIL-101 are given.

Compound	Slope [1/ns]	Stand. error slope [1/ns]	R ² -value	Lifetime [ns]	Lifetime error [ns]
CdS@MIL-101	-3.001	0.018	0.99881	0.333	0.002
CdS/TiO ₂ @MIL-101	-3.346	0.043	0.99131	0.299	0.004
Ni/CdS/TiO ₂ @MIL-101	-4.238	0.032	0.99711	0.236	0.002

Photocatalytic Experiments

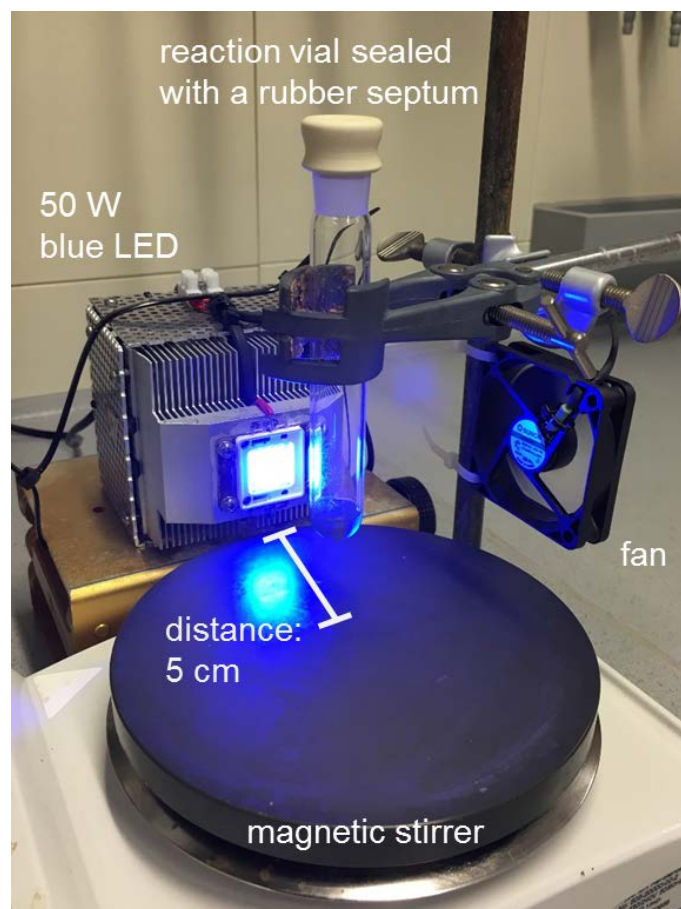
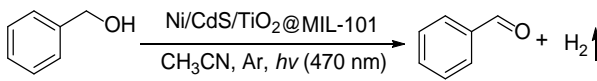


Figure S9. Experimental setup for photocatalytic experiments. The reaction vials sealed with a rubber septum were illuminated by a 50 W blue LED (470 nm, distance 5 cm, ~15000 lx), stirred magnetically, and cooled by a fan.

We performed control experiments to investigate whether O_2 is inserted into the reaction vials by diffusion through the rubber septa during catalysis. Therefore, we prepared several experiments in a nitrogen-filled glovebox using the same amount of catalyst, substrate, and solvent as described in the supplementary methods section and sealed the reaction vials with a greased glass plug. The yields of the reactions prepared in the glove box were equal to the yields prepared according to the supplementary methods section using a rubber septum. Consequently, no entry of O_2 was observed, which would have influenced the reactions (for example the yields). Additionally, no entry of O_2 was observed during the analysis of the evolved amount of H_2 by GC-TDC.

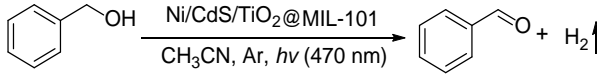
Table S3. Solvent screening for the photocatalytic dehydrogenation of benzyl alcohol.^[a]


c1ccc(cc1)CO >> c1ccc(cc1)C=O + H2
Ni/CdS/TiO₂@MIL-101
CH₃CN, Ar, *hν* (470 nm)

Entry	Solvent	Yield ^[b] [%]
1	Diglyme	14
2	Acetonitrile	53
3	Toluene	34
4	Tetrahydrofurane	12
5	Dimethoxyethane	15
6	1,4-Dioxane	6
7	No solvent	33

[a] Reaction conditions: 0.20 mmol Benzyl alcohol, 0.5 mg Ni/CdS/TiO₂@MIL-101, Ar, 0.30 mL solvent, 27 °C, 20 h, 470 nm blue LED 50 W. [b] Determined by GC using n-dodecane as internal standard.

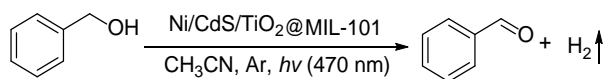
Table S4. Screening of the Ni amount for the photocatalytic dehydrogenation of benzyl alcohol.^[a]


c1ccc(cc1)CO >> c1ccc(cc1)C=O + H2
Ni/CdS/TiO₂@MIL-101
CH₃CN, Ar, *hν* (470 nm)

Entry	Catalyst ^[c]	Yield ^[b] [%]
1	Ni/CdS/TiO ₂ @MIL-101 (2 wt% Ni)	64
2	Ni/CdS/TiO₂@MIL-101 (4 wt% Ni)	73
3	Ni/CdS/TiO ₂ @MIL-101 (6 wt% Ni)	52

[a] Reaction conditions: 0.3 mmol benzyl alcohol, 0.5 mg catalyst, 0.5 mL solvent, Ar, 24 h, 27 °C, 470 nm blue LED 50 W. [b] Determined by GC using n-dodecane as internal standard. [c] The Ni content was calculated based on the amount of precursor.

Table S5. Catalyst screening for the photocatalytic dehydrogenation of benzyl alcohol.^[a]



Entry	Catalyst	Yield ^[b] [%]
1	Ni/CdS/TiO₂@MIL-101	73
2	Pd/CdS/TiO ₂ @MIL-101	16
3	Pt/CdS/TiO ₂ @MIL-101	21
4	Au/CdS/TiO ₂ @MIL-101	8
5	CdS/TiO ₂ @MIL-101	13
6	CdS@MIL-101	6
7	Ni/CdS@MIL-101	29
8	Ni/TiO ₂ @MIL-101	0
9	MIL-101	0
10	CdS ^[c]	5
11	Ni/CdS ^[c]	15
12	Ni/CdS ^[c] + TiO ₂ ^[d]	10
13	Ni/TiO ₂	0
14	Ni + CdS ^[c] + TiO ₂ ^[d]	6
15	Ni/CdS/TiO ₂ ^[d]	21
16	TiO ₂ (P25)	0

[a] Reaction conditions: 0.3 mmol benzyl alcohol, 0.5 mg catalyst, 0.5 mL solvent, Ar, 24 h, 27 °C, 470 nm blue LED 50 W. [b] Determined by GC using n-dodecane as internal standard. [c] Commercial available cubic CdS. [d] Commercial available TiO₂ (anatase).

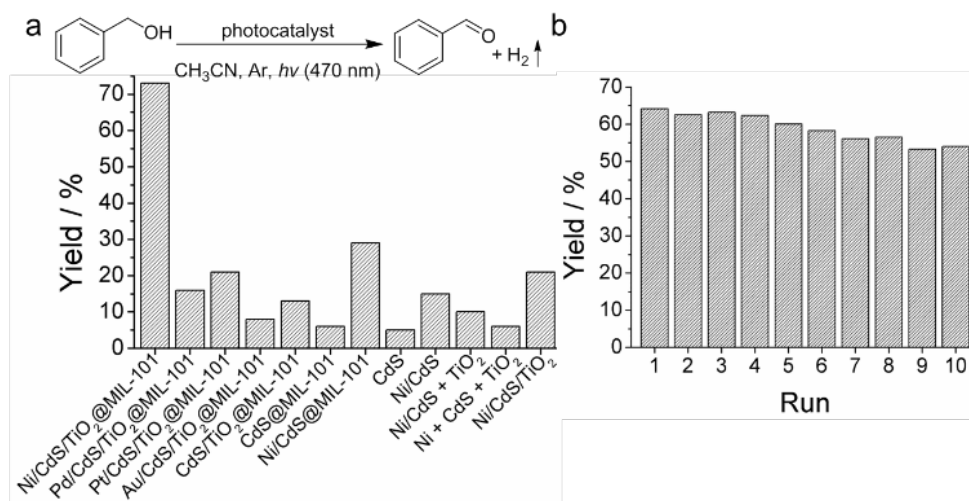


Figure S10. a) Comparison of different photocatalysts for the dehydrogenation of benzyl alcohol. The yields were determined by gas chromatography (GC) using n-dodecane as internal standard. b) Reusability of the Ni/CdS/TiO₂@MIL-101 catalyst with an activity decrease of less than 10 % after ten runs resulting from the purification procedure of the catalyst between the runs.

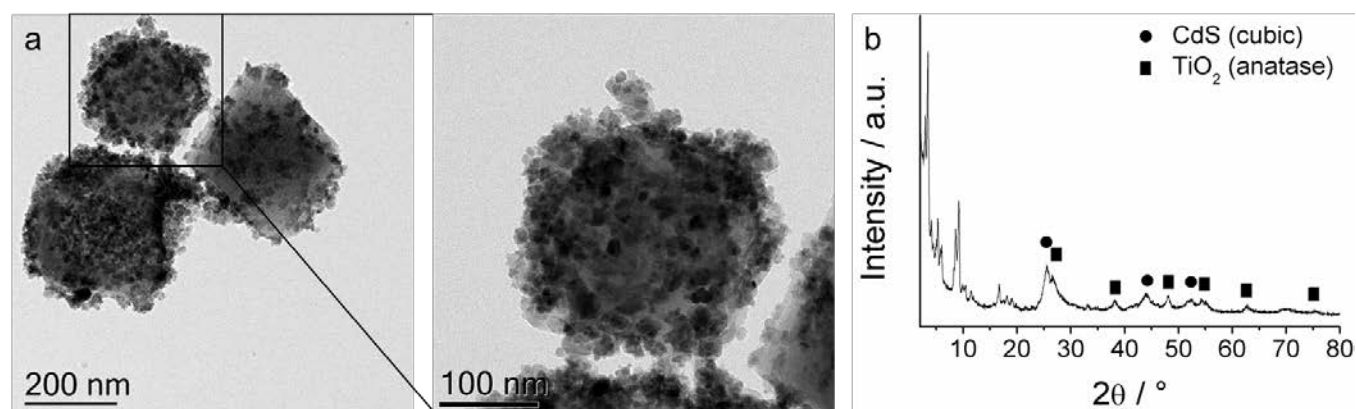


Figure S11. a) TEM micrographs of the Ni/CdS/TiO₂@MIL-101 catalyst reused for the photocatalytic dehydrogenation of benzyl alcohol for ten runs. b) XRD analysis of the reused catalyst.

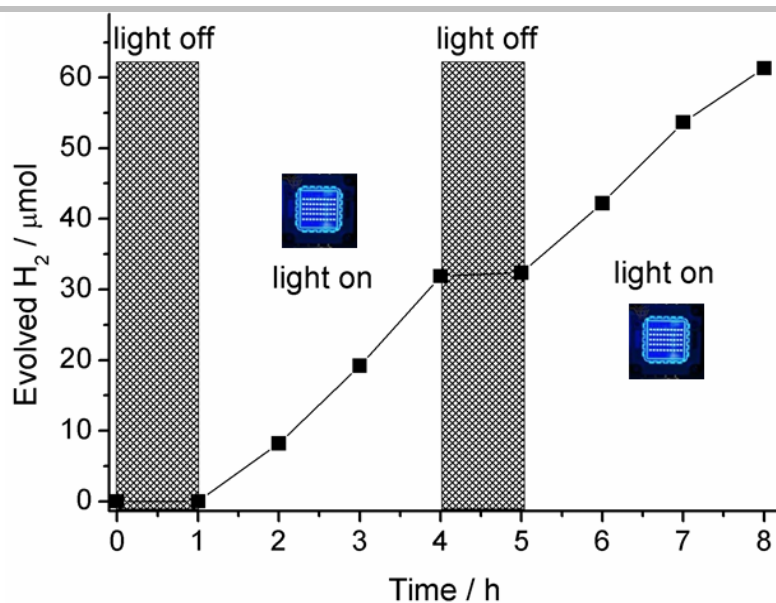


Figure S12. Light on/off experiment. Hydrogen evolution from benzyl alcohol was only observed under light illumination (4.0 mg Ni/CdS/TiO₂@MIL-101, 0.3 mmol benzyl alcohol, 0.3 mL CH₃CN, Ar, 50 W blue LED).

Table S6. Photocatalytic dehydrogenation of additional alcohols.^[a]

$$\text{R}'\text{-CH(OH)-H} \xrightarrow[\text{CH}_3\text{CN, Ar, } h\nu (470 \text{ nm})]{\text{Ni/CdS/TiO}_2\text{@MIL-101}} \text{R}'\text{-CHO} + \text{H}_2\uparrow$$

Entry	Product	R	Yield ^[b] [%]
1		R ¹ = OMe, R ² = H	>99
2		R ¹ = H, R ² = OMe	93
3		R ¹ = Me, R ² = H	>99
4		R ¹ = H, R ² = Me	82
5		R ¹ = F, R ² = H	87
6		R ¹ = Cl, R ² = H	>99
7 ^[c]		R ¹ = H, R ² = Cl	87
8 ^[c]		R ¹ = Br, R ² = H	96
9 ^[c]		R ¹ = OH, R ² = H	83
10		R ¹ = H, R ² = OH	87
11 ^[d]		R ¹ = H, R ² = CF ₃	89
12 ^[c]			78
13			85
14 ^[d]			92
15 ^[d]			83
16 ^[e]	acetone		64 ^[f]

[a] Reaction conditions: 0.1 mmol alcohol, 0.6 mg Ni/CdS/TiO₂@MIL-101, Ar, 0.3 mL CH₃CN, 27 °C, 24 h, 470 nm blue LED 50 W. [b] Determined by GC using n-dodecane as internal standard. [c] 1.2 mg Ni/CdS/TiO₂@MIL-101. [d] 1.2 mg Ni/CdS/TiO₂@MIL-101, 48 h. [e] Without solvent, 72 h. [f] Determined by the evolved amount of H₂ using methane as internal standard (GC-TCD).

Table S7. Hydrogen generation via photocatalytic dehydrogenation of alcohols.^[a]

$$\text{R}'\text{-CH(OH)-R}'' \xrightarrow[\text{CH}_3\text{CN, Ar, } h\nu (470 \text{ nm})]{\text{Ni/CdS/TiO}_2\text{@MIL-101}} \text{R}'\text{-C(=O)-R}'' + \text{H}_2\uparrow$$

Entry	Product	R	Yield ^[b] [μmol]	H ₂ ^[c] [μmol]
1		R ¹ = H, R ² = H	97	92
2		R ¹ = OMe, R ² = H	96	88
3		R ¹ = Cl, R ² = H	97	85
4			93	77
5			88	78
6		R ¹ = H, R ² = H	>99	93
7		R¹ = H, R² = H	10^[d]	0^[d]
8		R ¹ = Me, R ² = H	>99	94
9		R ¹ = H, R ² = NH ₂	96	84
10		R ¹ = OH, R ² = H	83	71

[a] Reaction conditions: 0.1 mmol alcohol, 0.6 mg Ni/CdS/TiO₂@MIL-101, Ar, 0.3 mL CH₃CN, 27 °C, 24 h, 470 nm blue LED 50 W. [b] Determined by GC using n-dodecane as internal standard. [c] Determined using methane as internal standard (GC-TCD). [d] Without inert atmosphere.

Table S8. Screening of the alcohol:amine ratio for the synthesis of imines.^[a]

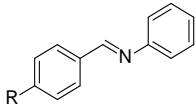

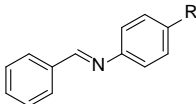
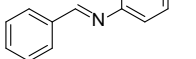
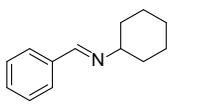
$$\text{C}_6\text{H}_5\text{CH}_2\text{OH} + \text{H}_2\text{N-C}_6\text{H}_5 \xrightarrow[\text{CH}_3\text{CN, Ar, } h\nu (470 \text{ nm})]{\text{Ni/CdS/TiO}_2\text{@MIL-101}} \text{C}_6\text{H}_5\text{CH=N-C}_6\text{H}_5 + \text{H}_2, \text{H}_2\text{O}$$

Entry	alcohol:amine	Yield ^[b] [%]
1	1:1	36
2	1.1:1	41
3	1.2:1	49
4	1.3:1	66
5	1.4:1	65

[a] 0.1 mmol aniline, benzyl alcohol, 1.5 mg Ni/CdS/TiO₂@MIL-101, Ar, 0.15 mL CH₃CN, 27 °C, 30 h, 470 nm blue LED 50 W. [b] Determined by GC using n-decane as internal standard.

Table S9. Hydrogen liberation during the photocatalytic synthesis of imines from alcohols and amines.^[a]

$$R'-CH_2OH + H_2N-R'' \xrightarrow[\text{-H}_2, \text{-H}_2\text{O}]{\text{Ni/CdS/TiO}_2\text{@MIL-101, CH}_3\text{CN, Ar, } h\nu \text{ (470 nm)}} R'-CH=N-R''$$

Entry	Product	R	Yield ^[b] [%]	H ₂ ^[c] [μmol]
1		R = H	92	113
2		R = H	50 ^[d]	0 ^[d]
3		R = Me	86	107
4		R = Cl	88	95
5		R = Me	88	107
6		R = OMe	93	117
7			87	113

[a] Reaction conditions: 0.1 mmol amine, 0.13 mmol alcohol, 1.5 mg Ni/CdS/TiO₂@MIL-101, Ar, 0.15 mL CH₃CN, 27 °C, 48 h, 470 nm blue LED 50 W. [b] Determined by GC using n-decane as internal standard. [c] Determined using methane as internal standard (GC-TCD). The benzyl alcohol derivatives (0.13 mmol) were completely oxidized to the corresponding aldehydes. [d] Without inert atmosphere.

Theoretical Procedures

The aim of the Density Functional Theory (DFT) calculations that we report in this supplemental information is to check in a transparent model calculation whether there is a difference in the strength with which a benzyl alcohol molecule binds to a Ni and a Pd particle. We believe that this comparison is most meaningful when the metal particles have a similar geometry. Therefore, we chose to compare the strength with which one benzyl alcohol molecule (C_7H_8O) binds to either Ni_{13} or Pd_{13} , with the latter having similar geometries that result from a basic icosahedral motive.

Our calculations use the TURBOMOLE^[S3] program package. Geometry optimizations (GO) serve to find reasonable nanoparticle structures. All GOs of the model system were carried out with the Perdew-Burke-Ernzerhof (PBE)^[S4,S5] generalized gradient approximation (GGA) and the def2-TZVP^[S6] basis set. The same basis set was also used in all calculations with a hybrid exchange-correlation (xc) functional (see below). All our calculations take *van-der-Waals'* interactions into account via the scheme of Grimme.^[S7]

Metals with d-electrons are challenging for many exchange-correlation energy approximations, because the inaccuracies of semi-local functionals affect localized and delocalized orbitals quite differently. One-electron self-interaction^[S8], e.g., depends sensitively on orbital localization.^[S9] Hence, studying systems containing Ni and/or Pd requires special care.^[S10] To make sure that the qualitative conclusions that we draw here are not affected by such errors, we check whether the trends that we observe with the PBE GGA are reproduced by the Becke-3-parameter-Lee-Yang-Parr (B3LYP)^[S11,S12] hybrid xc functional that cancels the self-interaction error partially due to its fraction of Fock exchange.

Table S10. Total energy $E_{\text{tot}}^{\text{xc}}$ of one benzyl alcohol (C_7H_8O), the bare metal particles ($Ni_{13}(\text{ico})$, $Pd_{13}(\text{ico})$) and the combined system Ni_{13}/C_7H_8O and Pd_{13}/C_7H_8O , respectively. Binding energies ΔE_B^{xc} are calculated based on the total energy differences according to equation (1) as described in the text. All numbers are in eV.

	$E_{\text{tot}}^{\text{PBE}}$	ΔE_B^{PBE}	$E_{\text{tot}}^{\text{B3LYP}}$	$\Delta E_B^{\text{B3LYP}}$
C_7H_8O	-9427.9455	–	-9434.3790	–
$Ni_{13}(\text{ico})$	-533506.0785	–	-533554.0148	–
$Pd_{13}(\text{ico})^{\text{[a]}}$	-45270.8245	–	-45250.4232	–
$Pd_{13}/C_7H_8O(\text{S13a})^{\text{[a,b]}}$	-54701.2921	-2.52	-54685.8137	-1.01

Pd ₁₃ /C ₇ H ₈ O(S13c) ^[a,b]	-54701.2740	-2.50	–	–
Ni ₁₃ /C ₇ H ₈ O(S13b) ^[b]	-542937.0146	-2.99	-542989.5710	-1.18
Ni ₁₃ /C ₇ H ₈ O(S13d) ^[b]	-542936.9670	-2.94	–	–
Pd ₁₃ /C ₇ H ₈ O(3a) ^[a,c,d1]	-54701.4167	-2.65	–	–
Pd ₁₃ /C ₇ H ₈ O ^[a,d2]	-54701.4140	-2.64	–	–
Ni ₁₃ /C ₇ H ₈ O(3b) ^[c,d1]	-542937.1477	-3.12	–	–
Ni ₁₃ /C ₇ H ₈ O ^[c,d2]	-542937.1368	-3.11	–	–

[a] relativistic Pd-effective-core-potential ^[S13]	[b] (S13x) refers to Figure S13 a, b, c, d	[c] (3x) refers to Figure 3 a, b	[d1] relaxed lowest energy structure from DFT BOMD	[d2] relaxed second lowest energy structure from DFT BOMD
---	--	----------------------------------	--	---

We started by doing GOs for one benzyl alcohol molecule and the 13-atom Ni and Pd clusters separately. Table S10 shows the corresponding total energies. Different structural isomers are reported in the literature for Ni₁₃^[S10,S14,S15] and Pd₁₃^[S10,S16,S17]. We started from the stable structures reported in refs. [S14] and [S10] for Ni₁₃ and Pd₁₃, respectively. From those we chose the icosahedral structure for both MNP clusters and relaxed the structure. Previous calculations found the icosahedral geometry as the Ni₁₃(ico) ground state.^[S10,S14] For Pd₁₃, the icosahedral geometry is stable as well, but PBE and PBE0 calculations favor a bilayered structure and a geometry showing *c3v* symmetry by circa 124 meV and 26 meV, respectively.^[S10,S16] In order to have a comparison on the same metal geometry, we chose the icosahedral geometry for Pd₁₃ as the basis of our study. This choice is further motivated by unpublished DFT Born-Oppenheimer-Molecular-Dynamics (BOMD) room-temperature data obtained by some of us in the context of another study that shows that an icosahedral Pd₁₃ cluster is stabilized by solvent molecules. Thus, we consider the icosahedral structure the more relevant one for the present study.

When determining the electronic structure of small Ni and Pd clusters, one must further take into account that they can show a non-zero magnetic moment.^[S10,S14,S15,S16,S17,S18,S19,S20,S21,S22] For Pd₁₃(ico) both PBE and PBE0 predict a spin magnetic moment of 8 μ_B for the ground state. For Ni₁₃(ico) the situation is different. PBE prefers 8 μ_B , yet PBE0 yields a higher magnetic state of 16 μ_B . Our results for both MNP clusters agree with refs. [S10, S14, S16] within the margins of comparability and reproducibility. In our study, we used the semi-empirical Becke-3-parameter-Lee-Yang-Parr (B3LYP)^[S11,S12] hybrid functional, which also lead to 16 μ_B ground state. The magnetic, high spin state predicted by hybrid functionals (PBE0, B3LYP), seems to conform with recent X-ray magnetic circular dichroism spectroscopy experiments of cationic Ni₁₃⁺ that were independently reported by Langenberg

et al.^[S18] and Meyer et al.^[S19]. Prior to these, however, Stern-Gerlach studies^[S20,S21] on Ni₁₃ predicted a lower total magnetic moment. For our calculation of the binding energies we therefore in each case used the lowest energy structures that we found.

Finally, we modeled a joint system, determined its total energy ($E_{\text{tot}}^{\text{xc}}$) and calculated the binding energy ($\Delta E_{\text{B}}^{\text{xc}}$) via

$$\Delta E_{\text{B}}^{\text{xc}} (\text{MNP}_{13}/\text{C}_7\text{H}_8\text{O}) = E_{\text{tot}}^{\text{xc}} (\text{MNP}_{13}/\text{C}_7\text{H}_8\text{O}) - E_{\text{tot}}^{\text{xc}} (\text{MNP}_{13}) - E_{\text{tot}}^{\text{xc}} (\text{C}_7\text{H}_8\text{O}), \quad (1)$$

where *xc* refers to the functional (here PBE and later B3LYP), MNP₁₃ to either Ni₁₃(ico) or Pd₁₃(ico) and MNP₁₃/C₇H₈O to the joint system. For each structure we carried out a set of GOs with fixed spin magnetic moments (in μ_{B}) in the range of [0,2,...,10] to determine its magnetic ground state. In this system, we started from a geometry in which the benzyl alcohol's benzene ring was close to the MNP and relaxed these initial structure (with PBE). We used different starting geometries, with the functional group (-OH) pointing towards or away from the MNP, respectively (Figure S13).

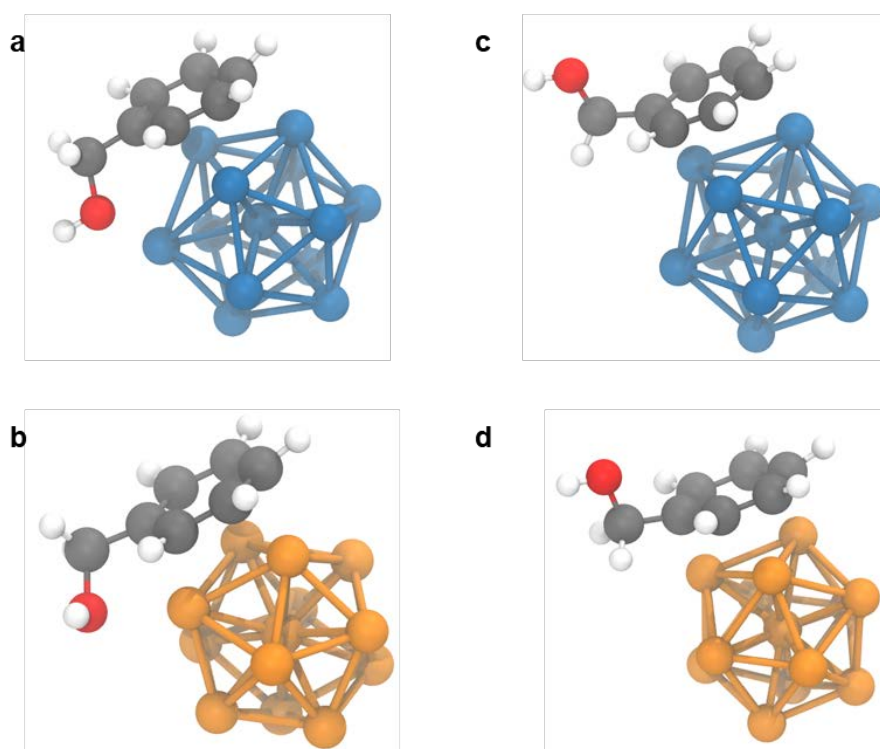


Figure S13. Relaxed structures with different arrangements of the functional group (-OH) of benzyl alcohol with respect to (top) Pd₁₃(ico) and (bottom) Ni₁₃(ico).

We found that with PBE the former is slightly preferred by both Ni₁₃/C₇H₈O and Pd₁₃/C₇H₈O by some 50 meV and only a few meV, respectively. The lowest energy configurations, corresponding to Figure S13 (a, b), showed a binding energy of 2.99 eV (Ni₁₃/C₇H₈O (8 μ_{B})) and 2.52 eV (Pd₁₃/C₇H₈O (4 μ_{B})), i.e., a difference of ca. 0.4 eV. Furthermore, comparing the magnetic moments of the joint

system to the bare 13-atom MNP clusters using the PBE functional shows a quenching of the magnetic moment for Pd₁₃/C₇H₈O (4 μ_B), but not for Ni₁₃/C₇H₈O (8 μ_B).

To check whether the observed trend in binding energy is robust we also computed the electronic structure with B3LYP. To this end, we kept the two aforementioned lowest energy geometries fixed (Figure S13 (a, b)) and carried out a ground state calculation. The spin magnetic moment (in μ_B) for these calculations was varied in the range of [0,2,...,8] and [0,2,...,16] for Pd₁₃/C₇H₈O and Ni₁₃/C₇H₈O, respectively. Our B3LYP ground state calculations yielded a binding energy of 1.18 eV (Ni₁₃/C₇H₈O degenerate 8 μ_B and 10 μ_B state) and 1.01 eV (Pd₁₃/C₇H₈O (4 μ_B)), respectively. For fixed geometries we thus find smaller binding energies with the hybrid functional, but the trend of stronger binding to Ni₁₃ is confirmed. The hybrid calculation also confirms the quenching of the magnetic moment for the Pd system, yet also predicts a reduction of the spin to a degenerate 8 and 10 μ_B state for the Ni system. An in-depth analysis of the magnetic moment for small MNP clusters will be part of a future study.

Finally, in order to check whether our locally optimized structures are realistic and to take into account potential temperature effects, we carried out a DFT BOMD simulation with a Nosé-Hoover thermostat.^[S23,S24] For this we used the following setup: The thermostat temperature was 298.15 K and the PBE xc functional was employed in combination with the def2-SVP^[S25] basis set. The presence of the substrate alters the relative permittivity (ε_R=13.5)^[S26] of the medium. We took this shift into account via the conductor-like screening model.^[S27] Based on our GO calculations, we chose a fixed spin magnetic moment of 8 μ_B and 4 μ_B for the Ni and Pd system, respectively. The relaxation time equaled approximately 13 fs (560 a.u.) and 9.3 fs (400 a.u.) for Pd₁₃/C₇H₈O and Ni₁₃/C₇H₈O, respectively. The time step was some 1.9 fs (80 a.u.) and the total simulation time was circa 3 ps, which was sufficient to observe several low energy structures. We extracted the two lowest energy structures from these BOMD calculations and further relaxed them with the same PBE setup as before. As a result, we found that Ni₁₃/C₇H₈O (8 μ_B) is bound by -3.11 to -3.12 eV and Pd₁₃/C₇H₈O (4 μ_B) by -2.64 to -2.65 eV. Thus, the binding energies observed for these new structures are larger than for the locally optimized ones, but the trend of stronger binding to Ni is again robust. The lowest energy conformations, i.e. those corresponding to -3.12 and -2.65 eV, are depicted in the main manuscript (Figure 3).

References

- [S1] J. Hermannsdörfer, M. Friedrich, R. Kempe, *Chem. Eur. J.* **2013**, *19*, 13652–13657.
- [S2] D. Tilgner, R. Kempe, *Chem. Eur. J.* **2017**, *23*, 3184–3190.
- [S3] TURBMOLE V7.3 **2018**, a development of University of Karlsruhe and Forschungszentrum Karlsruhe GmbH, 1989-2018.
- [S4] J. P. Perdew, K. Burke, M. Ernzerhof, *Phys. Rev. Lett.* **1996**, *77*, 3865-3868.
- [S5] J. P. Perdew, K. Burke, M. Ernzerhof, *Phys. Rev. Lett.* **1997**, *78*, 1396.
- [S6] A. Weigend, R. Ahlrichs, *Phys. Chem. Chem. Phys.* **2005**, *7*, 3297–3305.
- [S7] S. Grimme, *Inc. J. Comput. Chem.* **2004**, *25*, 1463–1473.
- [S8] J. P. Perdew, Alex Zunger, *Phys. Rev. B* **1981**, *23*, 5048-5079.
- [S9] T. Körzdörfer, S. Kümmel, N. Marom, L. Kronik, *Phys. Rev. B* **2009**, *79*, 201205.
- [S10] L. Leppert, R. Kempe, S. Kümmel, *Phys. Chem. Chem. Phys.* **2015**, *17*, 26140-26148.
- [S11] A. D. Becke, *J. Chem. Phys.* **1993**, *98*, 5648-5652.
- [S12] P.J. Stephens, F. J. Devlin, C. F. Chabalowski, M. J. Frisch, *J. Phys. Chem.* **1994**, *98*, 11623-11627.
- [S13] D. Andrae, U. Haeussermann, M. Dolg, H. Stoll, H. Preuss, *Theor. Chim. Acta* **1990**, *77*, 123-141.
- [S14] G. L. Gutsev, C. W. Weatherford, K. G. Belay, B. R. Ramachandran, P. Jena, *J. Chem. Phys.* **2013**, *138*, 164303.
- [S15] J. P. Chou, C. R. Hsing, C. M. Wei, C. Cheng, C. M. Chang, *J. Phys.: Condens. Matter* **2013**, *25*, 125305.
- [S16] A. M. Köster, P. Calaminici, E. Orgaz, D. R. Roy, J. U. Reveles, S. N. Khanna, *J. Am. Chem. Soc.* **2011**, *133*, 12192-12196.
- [S17] B. Fresch, H.-G. Boyen, F. Remacle, *Nanoscale* **2012**, *4*, 4138–4147.
- [S18] A. Langenberg, K. Hirsch, A. Ławicki, V. Zamudio-Bayer, M. Niemeyer, P. Chmiela, B. Langbehn, A. Terasaki, B. v. Issendorff, J. T. Lau, *Phys. Rev. B* **2014**, *90*, 184420.
- [S19] J. Meyer, M. Tomber, T. van Wüllen, G. Niedner-Schattenburg, S. Peredkob, W. Eberhardt, M. Neeb, S. Palutke, M. Martins, W. Wurth, *J. Chem. Phys.* **2015**, *143*, 104302.
- [S20] M. B. Knickelbein, *J. Chem. Phys.* **2002**, *116*, 9703-9711.
- [S21] S. E. Apsel, J. W. Emmert, J. Deng, L. A. Bloomfield, *Phys. Rev. Lett.* **1996**, *76*, 1441-1444.
- [S22] A. J. Cox, J. G. Louderback, S. E. Apsel, L. A. Bloomfield, *Phys. Rev. B* **1994**, *49*, 12295-12298.
- [S23] W. G. Hoover, *Phys. Rev. A* **1985**, *31*, 1695–1697.
- [S24] S. Nosé, *J. Chem. Phys.* **1984**, *81*, 511–519.
- [S25] A. Schäfer, H. Horn, R. Ahlrichs, *J. Chem. Phys.* **1992**, *97*, 2571–2577.
- [S26] Ch. Wohlfart, Landolt-Börnstein (Supplement to IV/6), **2008**, *17*, 396-396.
- [S27] A. Klamt, G. Schuurmann, *J. Chem. Soc.* **1993**, *2*, 799–805.